Check for updates

Solar RRL

RESEARCH ARTICLE

In-situ Dual-stage Reactions Enhance Operational Stability of High-Efficiency Perovskite Modules

Jialiang Liu[1] | Mengjie Li[2] | Jinxi Zheng[1] | Hao Huang[1] | Zhiguo Zhao[2] | Meicheng Li[1]

[1]State Key Laboratory of Alternate Electrical Power System with Renewable Energy Sources, School of New Energy, North China Electric Power University, Beijing, China | [2]China Huaneng Clean Energy Research Institute, Beijing, China

Correspondence: Hao Huang (hhuang@ncepu.edu.cn) | Zhiguo Zhao (zg_zhao@qny.chng.com.cn) | Meicheng Li (mcli@ncepu.edu.cn)

Received: 26 February 2026 | **Revised:** 8 April 2026 | **Accepted:** 15 April 2026

Keywords: in situ reaction | interface | perovskite solar modules | redox | stability

ABSTRACT

A critical perquisite for the commercialization of perovskite photovoltaics lies in the development of high-efficiency perovskite solar modules (PSMs) with long-term operational stability. Herein, we report in situ dual-stage surface reaction engineering, by introducing a multifunctional 3-amino-4-mercapto(trifluoromethyl)benzene hydrochloride (ATB), to enhance operational stability in high-performance PSMs. Initially, the ATB selectively reacts with surface formamidinium ions, reducing the perovskite defects and inducing an n-type doping that corresponds to an optimized interfacial energy level match. Subsequently, the thiol groups with redox properties in ATB initialize a reaction cycle between I_2 and Pb^0 generated during the operational aging of perovskite device, thus suppressing the defect accumulation and enhancing the device operational stability. As a consequence, the PSMs achieved PCEs of 23.3% (11.2 cm^2, aperture area) and 21.2% (694.5 cm^2, aperture area), with exceptional operational stability retaining > 99% of their initial PCE after 2000 h under continuous 1-sun illumination at 25°C and > 90% PCE following 1600 h at 85°C.

1 | Introduction

The metal halide perovskite materials possess optimal photoelectrical properties such as high absorption coefficient, long carrier lifetime, etc. for fabricating high-efficiency solar cells [1]. At present, the single junction perovskite solar cells have achieved certified power conversion efficiencies (PCE) exceeding 27% in lab-scale devices [2, 3], highlighting the tremendous potential toward industrialization and commercialization. However, there are unavoidable challenges that lie in the manufacturing technology for the large-area perovskite solar modules (PSMs) and prolong the device operation stability [4–11]. The cell-to-module efficiency gap is evidenced by the markedly reduced PCEs of small-area devices (>26% for approximately 1 cm^2) and large-area modules (>23% for approximately 100 cm^2) [12, 13]. Compounding this issue, most perovskite modules lose more than 20% efficiency per annum [14]. Without a systematic strategy focusing on both PSM efficiency and durability, perovskite photovoltaics risk remaining laboratory achievements rather than world-changing energy technologies.

The efficiency gap is progressively narrowing due to substantial advancements in light-absorbing layers, charge transport layers, interfacial engineering, and scalable fabrication techniques [15–20]. For example, Liu et al. modify the perovskite/ETL interface by nonpolar solvent-soluble non-fullerene acceptor, achieving certified PCEs of 23.05%, 22.32%, and 21.1% for inverted PSMs with active areas of 50 cm^2, 400 cm^2, and 1160 cm^2, respectively [17]. Wang et al. enabled the production of 7200 cm^2 PSMs that achieved a certified efficiency of 17.2% through solvent adjustment and a confinement edge-protection strategy [18]. The quantifiable nature of PCE coupled with its rapid advancement encouraged the academic interest and social attention mainly focusing on PCE progress, neglecting the challenges posed by stability to a certain extent [21]. In current, considering that the PSM efficiency basically meet the industrialization threshold, operational stability remains a critical issue. Although recent efforts in the perovskite photovoltaics research community have begun to focus on degradation mechanisms and durability testing, these efforts remain much rarer than those exploring

© 2026 Wiley-VCH GmbH.

efficiency. Various techniques have been employed to enhance the stability of PSMs, including composition engineering, defect passivation, barrier layer fabrication, and stable transport layer deposition [21–25]. However, the operational durability of PSMs remains constrained, necessitating further in-depth investigation and comprehensive resolution. Therefore, it is necessary to develop novel strategy to effectively enhance the PSC operational stability which possess a distinct mechanism from the PSM efficiency improvement, realizing the high-performance and long-term operational stable PSMs [26, 27].

Herein, we introduced a multifunctional 3-amino-4-mercapto(-trifluoromethyl)benzene hydrochloride (ATB) on the perovskite surface to construct a two-stage in situ reaction, attempting to enhance the PSM operational stability and improve its efficiency. First, the ATB selectively reacts with surface formamidinium (FA) ions during the process stage, which can reduce the surface roughness and passivate the defects. This reaction can also induce a n-type doping with reduced surface work function, optimizing the interface energy level match. Second, the thiol groups with redox properties in ATB initialize a reaction cycle between I_2 and Pb^0 during the PSM aging, thus continuously suppressing the defect accumulation, which effectively enhance the PSM operational stability. As a result, the PSMs with aperture area of 11.2 cm^2 and 694.5 cm^2 achieved PCEs of 23.3% and 21.2%, respectively. Moreover, the PSMs possess enhanced operational stability by retaining > 99% of their initial PCE after 2000 h under continuous 1-sun illumination at 25°C and > 90% PCE following 1600 h at 85°C.

2 | Results and Discussion

2.1 | Dual-Stage Surface Reaction

One of the reasons for the cell to module efficiency loss is the increased defect state density during upscaling. In particular, interfaces exhibit high defect densities, low energy barriers for ion migration, and susceptibility to moisture- and oxygen-induced degradation [4, 5]. During the processing of perovskite film, the film surface is vulnerable to generate defect considering the escape of volatile species such as organic molecules and iodine, which makes the top-surface engineering to be particularly important to enhance the performance of the PSMs. We design an in situ dual-stage surface reaction engineering to regulate the top surface through introducing a molecule (ATB used in this work) with active amino and thiol functional groups. We first describe the surface reaction between FA^+ and ATB, which is mainly occurred during the post-treatment of perovskite film. Figure 1a illustrates the detailed reaction pathway with the product of 4-(trifluoromethyl)-2-thioguanidine (TFPFA). Specifically, the amino group in ATB initiates the condensation reaction through nucleophilic attack on the imine carbon of FA, which is subsequently followed by an intramolecular rearrangement process, ultimately yielding the target product TFPFA. We carried out the electrostatic potential (ESP) of the ATB molecule using the calculation of density functional theory (DFT) to analyze the electron density distribution and reactivity of its active sites. As shown in Figure S1, the —CF_3 group displays evident negative ESP due to its strong electron-withdrawing effect. The —SH group is located in the position opposite to the —CF_3 group. The electron cloud density around the sulfur atom is drawn toward the —CF_3 group, resulting in the absence of significant positive ESP on the sulfur atom, while the redox reactivity of the —SH bond is preserved. This reduces the reactivity of the —SH group toward surface defects. However, the hydrogen atoms on the —NH_2 group exhibit a positive ESP. This positively charged —NH_2—H can be regarded as a potential active site for reacting with FA^+ ions.

As shown in Figure 1b, the thermogravimetric analysis (TGA) curve evaluates the thermal stability of FAI, ATB, and their mixture (FAI + ATB) under an inert atmosphere. The mixture of FAI + ATB exhibits a distinct thermal behavior compared to the individual components, indicating a potential interaction between FAI and ATB [28]. We further performed proton nuclear magnetic resonance (^{1}H NMR) spectroscopy to demonstrate the reaction between FA + and ATB with the results shown in Figure 1c. For pure ATB, a characteristic signal at ∼ 7.5 ppm corresponds to the aromatic —NH_2 proton. FAI exhibits distinct peaks at ∼ 7.8 ppm and ∼ 8.5 ppm, corresponding to its —NH and imine —CH=protons, respectively [23, 29]. Notably, the mixture of FAI + ATB displays several new peaks that are absent in the individual components. A new resonance at ∼ 5.5 ppm, possibly assigned to the C—NH—C of the target product TFPFA, arises from the secondary amine proton within the guanidine of TFPFA. The peaks at ∼ 7.0 ppm and ∼ 8.0 ppm are attributed to the imine —CH=proton and the terminal —NH proton of TFPFA, respectively. The disappearance of the original ATB —NH_2 signal and the shift of FAI —NH resonance further support the formation of the TFPFA. The Fourier transform infrared (FTIR) spectra of FAI, ATB, and FAI + ATB at room temperature are shown in Figure S2. The characteristic —NH and C=N stretching peaks of FAI exhibit distinct shifts toward higher wavenumbers after interaction with ATB. In FTIR spectroscopy, a peak shift to higher wavenumbers corresponds to an increase in bond strength, indicating that the —NH_2 group of ATB undergoes a condensation reaction with FA^+. The X-ray photoelectron spectroscopy (XPS) analysis shown in Figure 1d reveals that the N 1s spectrum of FAI exhibits a dominant peak at ∼ 400.0 eV, corresponding to the C=NH of FA^+. In contrast, the characteristic peak in the mixture of FAI + ATB exhibits a minor shift toward lower binding energy, positioned at approximately 399.5 eV, while an additional peak emerges at around 402.5 eV. The increased binding energy component indicates a reduced electron density around the specific nitrogen atoms in the newly formed product, which is consistent with the C—NH—C structure [23]. This observation further supports that the reaction product is TFPFA. In the C 1s spectrum (Figure S3), upon the introduction of ATB, the intensity of the characteristic peak corresponding to C—NH_2 significantly decreased, which may be attributed to the strong bonding interaction formed between the —NH_2 group in ATB and FA^+ [30]. The S 2p spectrum shows negligible significant binding energy shift, which indicates that the —SH groups remain chemically inert and do not participate in the coordination interaction (Figure S4).

Although the —SH group is not involved in the first-stage reaction, its dominates the second-stage redox reaction with the generated I_2 and Pb^0 during device aging. The —SH group is a highly redox-active moiety, and its representative redox behavior is the reversible conversion between thiols (R—SH) and disulfide bonds (R—S—S—R). This reversible conversion can induce a redox reaction cycle to reduce the I_2 and Pb^0. Figure 1e illustrates the redox

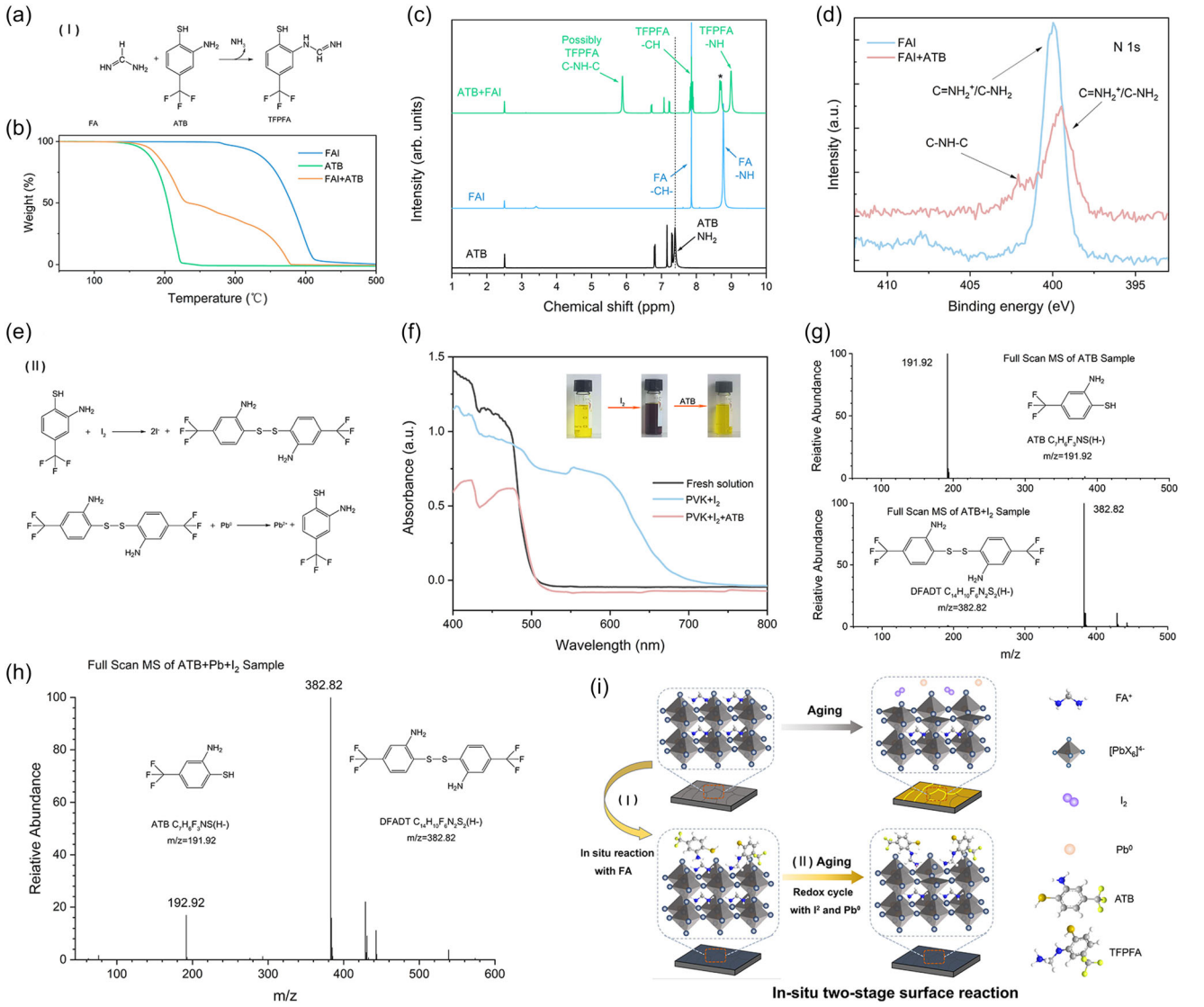


FIGURE 1 | (a) The chemical reaction equations for ATB and FA. (b) TGA curves of FAI, ATB, and FAI + ATB. (c) ^{1}H NMR spectra of FAI, PbI_2, FAI + ATB complex. (d) Binding energy of the N 1s of the FAI and FAI + ATB. (e) The chemical reaction equations for ATB + I_2 and ATB + Pb^0. (f) UV–vis absorption spectra of perovskite precursor solutions with different additives. Subfigure is the optical images showing the functions of MPAA in I_2 reduction. (g) ESI mass spectra of ATB and ATB + I_2 in methyl alcohol. (h) ESI mass spectra of ATB and ATB + I_2+Pb in methyl alcohol. (i) Schematic diagram illustrating the inhibiting perovskite film aging mechanism with ATB.

reaction process between ATB and the Pb^0 and I_2 generated after aging decomposition. Specifically, ATB or TFPFA reduces I_2 to I^- simultaneously undergoing oxidation to form a disulfide compound. Subsequently, this disulfide compound can oxidize Pb^0 to Pb^{2+}, while it is reduced back to ATB or TFPFA. The reversible conversion mechanism between the thiol group and the disulfide bond enables the redox mediator to regenerate itself while eliminating I_2 and Pb^0. We use the ATB as the example to detailly demonstrates this redox reaction cycle. Figure 1f supports that the ATB can reduce iodine. Initially, I_2 was added to the perovskite precursor solution at a 1:1 molar ratio relative to Pb^{2+}. After stored for 30 s, the solution shows a distinct color change from yellow to dark brown, indicating the presence of molecular I_2. Subsequently, ATB was introduced into the solution at a 1:2 molar ratio relative to I_2, and upon continued shaking, the solution rapidly reverted to its original yellow color. This observation aligns with the UV–vis spectral evolution of the perovskite precursor solution. Upon introduction of I_2 into the perovskite solution, significant shifts in the absorption band within 500–700 nm were observed. Notably, the ATB restored the absorption profile to nearly identical characteristics of the fresh solution. Figure S5 further demonstrates that the solution of ATB, I_2, and Pb changes from the deep reddish-brown to a light-yellow color after stirring for 30 s, with formed yellow precipitates which is evidenced to be PbI_2 at the bottom (Figure S6), further validating the reaction among the ATB, I_2, and Pb^0. Moreover, we employed the mass spectrum to validate this reaction process. As shown in Figure 1g, a single peak at $m/z = 191.92$ corresponds to the protonated ATB molecule $C_7H_6F_3NS$ (H^-). For the mixture of ATB + I_2, a peak at $m/z = 382.82$ is assigned to a dimer bridged by a disulfide bond $C_{14}H_{12}F_6N_2S_2$ (H^-), confirming oxidation of the —SH group to form —S—S— bonds. Figure 1h shows the spectrum of ATB + I_2+Pb, where peaks at $m/z = 191.92$ (ATB monomer) and $m/z = 382.82$ coexist. This supports the redox cycling process

where ATB monomers be oxidized to disulfide dimers, which are subsequently reduced back to monomers by Pb^0. Based on the mentioned dual-stage surface reaction, Figure 1i illustrates the mechanism by which ATB inhibits the degradation of perovskite films. Initially, the ATB selectively reacts with surface FA^+ to reduce the perovskite defects. Subsequently, the thiol groups with redox properties in ATB initialize a reaction cycle between I_2 and Pb^0 generated during the operational aging of perovskite device, thus suppressing the defect accumulation and enhancing the device operational stability.

2.2 | Optimization of Perovskite Film

To explore the influence of ATB treatment on perovskite film, we firstly performed the measurement of the scanning electron microscopy (SEM). Figure 2a,b shows the surface morphology of perovskite films without and with ATB passivation, respectively. The surface of the ATB-treated perovskite film appears somewhat blurred and a much smoother surface, suggesting that ATB molecules have formed a uniform coating on the surface and reconstructed the surface through reaction, which effectively passivates defects and enhances surface uniformity, considering the latter reaction of dual-stage reaction is associated with decomposition species of I_2 and Pb^0. Therefore, the reaction for the surface reconstruction and optimization should be the reaction between ATB with FA^+. The results of atomic force microscopy (AFM) reveal that the root-mean-square roughness (Rq) values are 15.9 nm for the untreated film and 12.2 nm for the ATB-treated film, confirming a moderate smoothing effect induced by surface reaction (Figure S7). To characterize the photoelectrical property of perovskite films, we performed PL mapping (Figure 2c) of perovskite films using a 520-nm laser by CCD camera. Compared to the control sample, the ATB-treated film exhibited stronger PL emission. We further employed point-by-point scanning on a large scale ($6 \times 6\ cm^2$) to test PL mapping (Figure S8). The perovskite film treated by ATB shows more stronger PL emission, which is consistent with the results of the previous test. This enhancement supports that the ATB can effectively reduce defect density and suppress the non-radiative

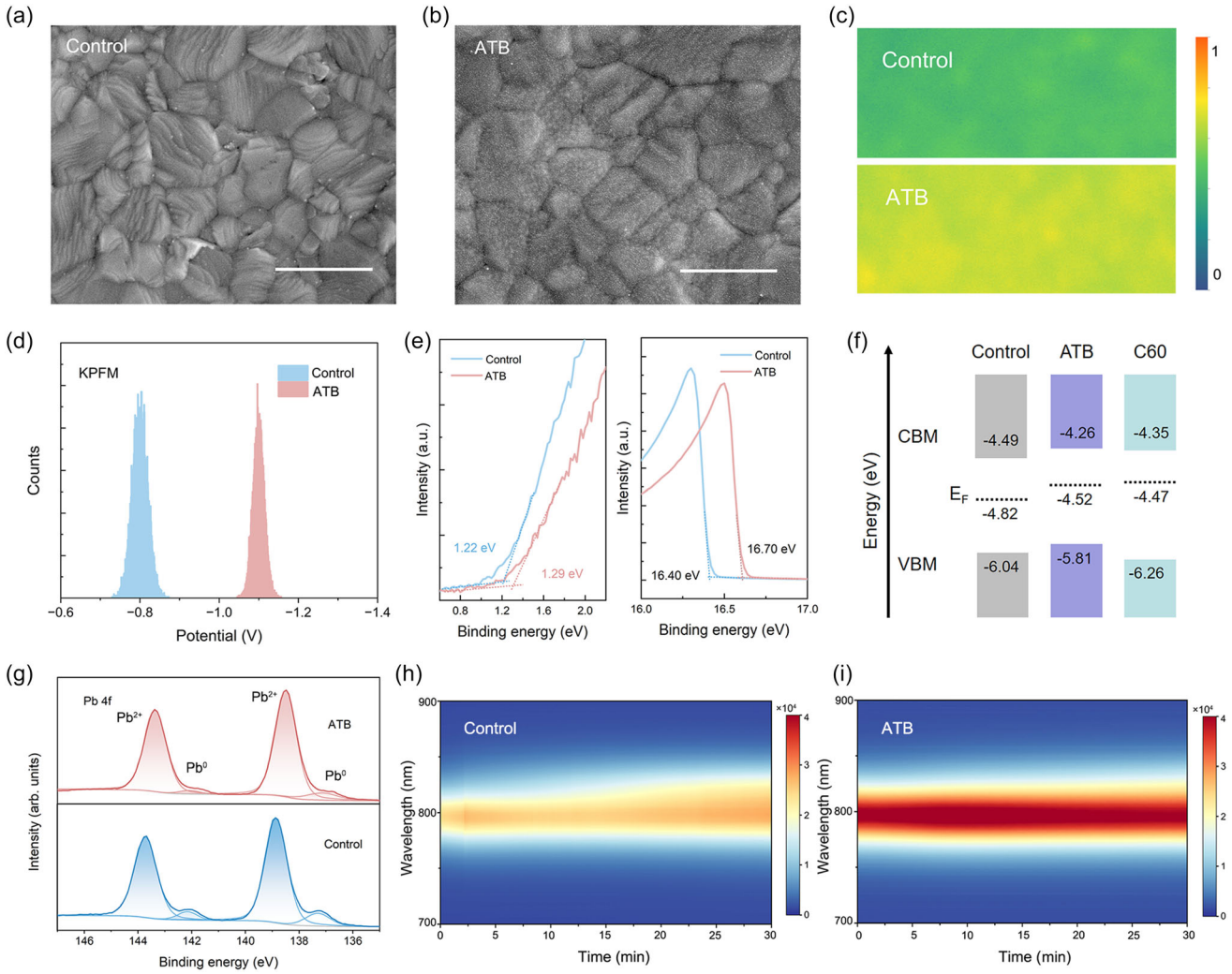


FIGURE 2 | SEM images of the perovskite film without (a) or with ATB (b). (c) PL mapping images of perovskite films without (top) or with ATB (bottom). Scale bars, 5 μm. (d) Histogram of surface potential distribution for the perovskite film without (control) or with ATB. (e) UPS spectra for perovskite films without and with ATB. (f) The energy band alignment diagram of perovskite without and with ATB, C60. (g) XPS spectra of Pb^0 in the perovskite films without (control) and with ATB after 30 min of ultraviolet illumination. In situ PL light stability of perovskite film without (h) and with ATB (i) by a 405 nm laser.

recombination. The results of time-resolved photoluminescence (TRPL) also validate the reduced defects density by ATB treatment (Figure S9).

In addition to reducing defect density, the ATB treatment also optimize the band energy alignment. The measurement of Kelvin probe force microscopy (KPFM) was performed to characterize the surface potential of perovskite films. As shown in Figure S10 and Figure 2d, the ATB-treated film displayed a more homogeneous surface potential distribution and a reduced surface potential compared to control film, indicating the induced reduction of surface work function [31]. The energy band structures of the perovskite films with or without ATB treatment and C60 were systematically investigated using ultraviolet photoelectron spectroscopy (UPS) with the results shown in Figure 2e and Figure S11. The UPS measurements revealed that ATB treatment reduces the work function of the perovskite film from 4.82 eV (control) to 4.52 eV. This reduction induces favorable energy band bending at the interface, which facilitates electron transport. The corresponding conduction band minimum (CBM) values were −4.49 eV and −4.26 eV for the control and ATB-treated films, respectively. By integrating these CBM values with the bandgap data obtained from external quantum efficiency (EQE) measurements which we mentioned in later parts, we constructed an energy band alignment diagram (Figure 2f). This diagram illustrates that the energy level difference in CBM between the ATB-treated perovskite film and the C60 film is diminished, indicating that the ATB significantly enhances the electron transfer at the perovskite/C60 interface.

We also characterized the stability of perovskite films. Considering the latter reaction of dual-stage reaction of ATB with perovskite film is associated with the I_2 and Pb^0, the species mainly generated after aging, we performed a harsh aging test on perovskite films under ultraviolet light irradiation. Figure 2g presents XPS spectrum of perovskite films after 30 min of ultraviolet illumination. The Pb^0 signal is nearly absent in the ATB-treated film, whereas a distinct peak persists in the control sample, supporting that ATB can effectively suppress metallic lead. In situ PL light stability of the perovskite film

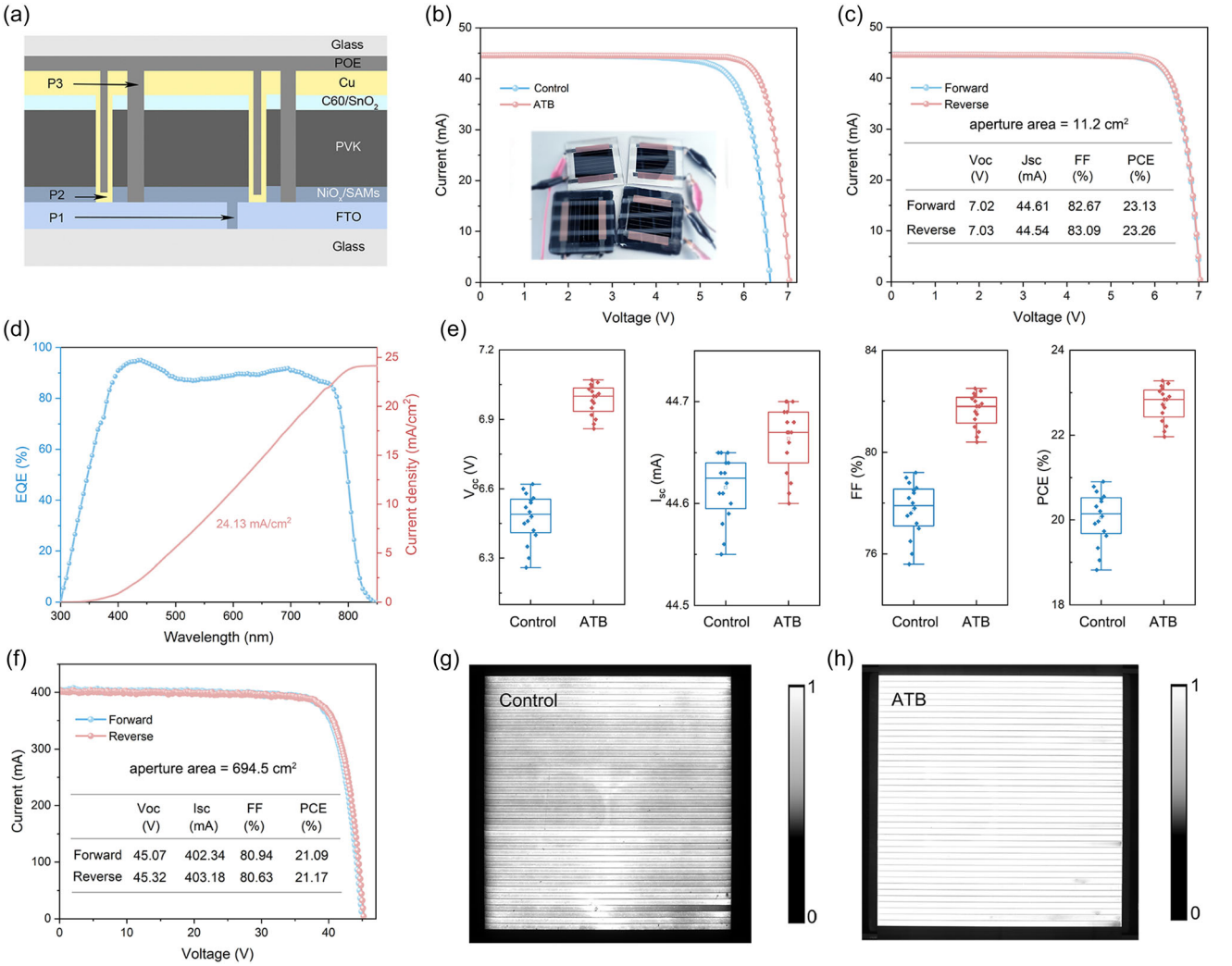


FIGURE 3 | Photoelectronic performance characterization of PSMs with or without ATB. (a) Schematic of device structure and laser scribing. (b) *I–V* curve of PSMs fabricated by ATB or control on a 6.7 × 6.7 cm^2 substrate. (c) The forward and reverse scans of the PSMs treated by ATB. (d) EQE spectra and integrated current density for the PSM treated by ATB. (e) Statistical distribution of module photovoltaic parameters (V_{OC}, J_{SC}, FF, and PCE) on the 6.7 × 6.7 cm^2 substrate. (f) *I–V* curve of PSMs fabricated by ATB on a 30 × 30 cm^2 substrate. (g) The EL images of PSMs on the 30 × 30 cm^2 FTO substrates without (g) and with ATB (h).

by a 405 nm laser was further tested, as shown in Figure 2h,i. The ATB-treated film shows superior stability compared to control, which also validate the enhanced stability of perovskite film.

2.3 | Photovoltaic Performance of PSMs

Building on the above studies of defect passivation and band energy alignment, we fabricated PSMs on $6.7 \times 6.7\ cm^2$ and $30 \times 30\ cm^2$ FTO substrates to verify its practicability. As shown in Figure 3a, the device architecture is FTO/NiO_x/SAMs/PVK/C60/SnO_2/Cu. The laser scribing dead zones (P1–P3) are 0.15 mm, resulting in a geometric fill factor (GFF) of 97%. All reported photovoltaic parameters correspond to encapsulated modules based on the perovskite composition $Cs_{0.07}MA_{0.05}FA_{0.88}PbI_3$. Figure 3b displays the current–voltage (I–V) curves for the $6.7 \times 6.7\ cm^2$ optimal devices under standard AM 1.5G illumination at 100 mW cm^{-2}. Impressively, the ATB devices exhibited a relatively high efficiency of 23.26%, whereas the control devices show lower efficiencies of 20.52%, primarily due to the decrease in open-circuit voltage (V_{OC}) and fill factor (FF). The champion PSM treated by ATB exhibits an V_{OC} of approximately 1.17 V and an FF exceeding 83.09%, with a steady-state efficiency of 23.26% (Figure 3c). In contrast, the control PSM shows a slight reduction in V_{OC} (1.10 V), a moderate decrease in FF (78%), and a reduced PCE (Figure S12). The EQE spectra in Figure 3d show that the champion PSM treated by ATB exhibits strong photo response over a wide absorption rang. The integrated J_{SC} values derived from the EQE curves are 24.13 mA/cm^2, which is consistent with the measured J_{SC} (24.63 mA/cm^2) in the I–V curves. Figure 3e shows the statistical distribution of PSM photovoltaic parameters (V_{OC}, I_{SC}, FF, and PCE). The average PCE, I_{SC}, V_{OC}, and FF of PSMs processed by ATB are higher than those of control, and the distribution is more concentrated, indicating better process reproductivity. We characterize the ideal factor and dark current of PSMs to analyze the reason for the efficiency improvement. The ATB-treated device exhibited an ideality factor of 1.27 kT/q, markedly lower than the 1.56 kT/q obtained from the control, which indicates the reduced non-radiative carrier recombination in the PSMs (Figure S13). This reduced non-radiative carrier

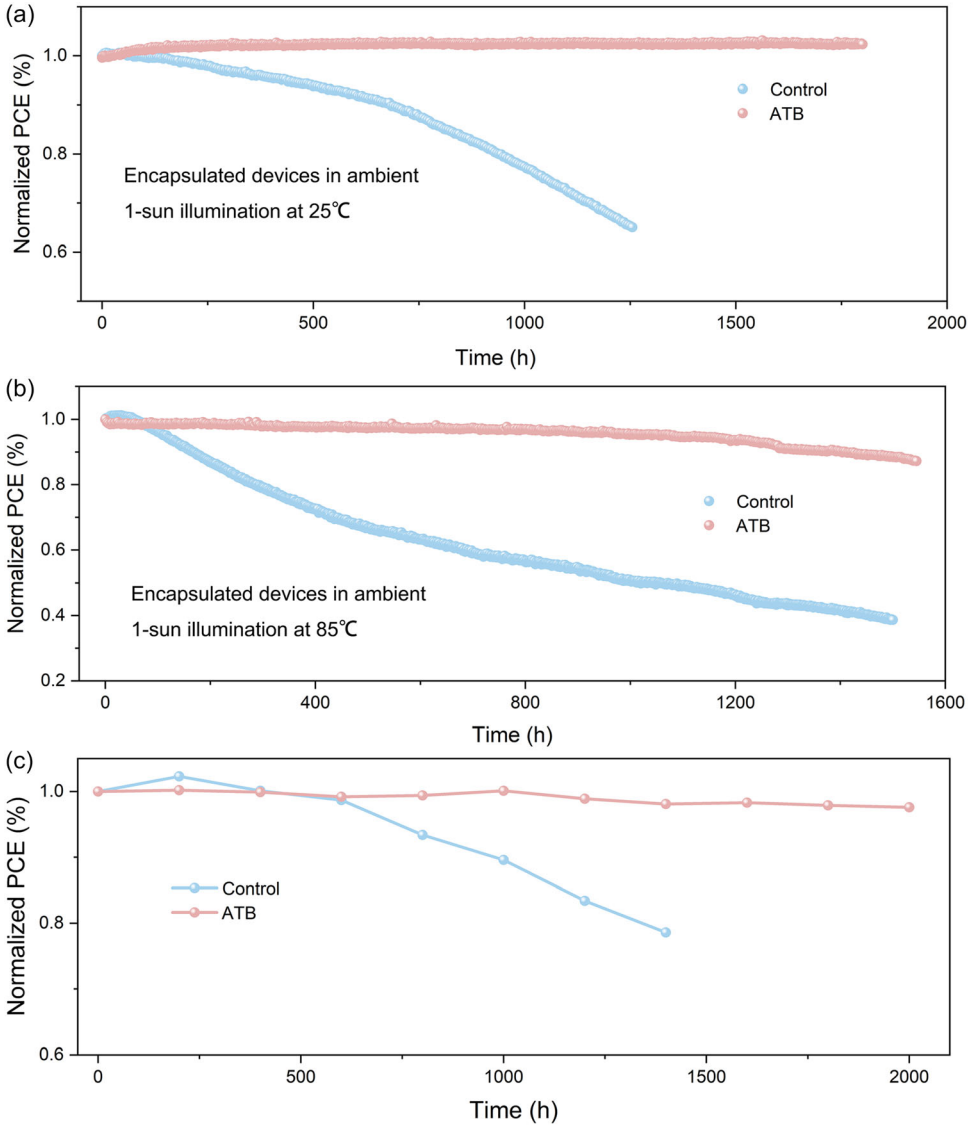


FIGURE 4 | Long-term light stability of encapsulated PSMs evaluated via MPPT under 1-sun equivalent illumination at 25°C (a) and 85°C (b). (c) The stability of encapsulated PSMs under 85°C/85% RH.

recombination can also be validated by the dark current suppression (Figure S14).

To evaluate the performance of ATB in larger-area devices, PSMs with an aperture area of 694.5 cm^2 were fabricated via slot-die coating on 30×30 cm^2 FTO substrates. Figure 3f presents the *I–V* curves of the champion PSM fabricated by ATB. The PSM exhibits an V_{OC} of approximately 1.11 V, a current of around 403 mA, and an FF exceeding 80.63%, yielding a PCE of 21.17%. The PCE for forward scan is 21.09%. The hysteresis index calculated based on the *I–V* measurements from forward and reverse scans is 0.38%. In contrast, as shown in Figure S15, the PCE of the control PSMs decreases to 18.23%, which is primarily attributed to the reduction in V_{OC} (1.03 V) and FF (78.61%). Concurrently, the hysteresis effect of the control perovskite module becomes increasingly prominent. Figure 3g,h shows the electroluminescence (EL) images of PSMs on the 30×30 cm^2 FTO substrates. The PSMs treated by ATB exhibit brighter and more homogeneous EL than the control device. This performance enhancement may be attributed to the optimized band energy alignment and improved interfacial electron transfer. Figure S16 presents the PCE of PSMs for different module areas. The red five-pointed star represents the efficiency obtained by ATB, and the blue sphere represents the efficiency reported in existing literature. The champion PSM exhibits a PCE close to the National Renewable Energy Laboratory (NERL) certified value of 21.1% at 843.5 cm^2. Moreover, the efficiency shows only a minor decline as the device area is scaled from 11.2 cm^2 (23.26%) to 694.5 cm^2 (21.17%), demonstrating outstanding scalability.

To further evaluate the operational stability of the devices, we conducted light-soaking aging tests on commercially encapsulated PSMs under maximum power point tracking (MPPT). As shown in Figure 4a, the ATB-treated devices exhibit excellent photostability under continuous 1-sun LED illumination at room temperature, retaining 99% of their initial PCE after 2000 h. Some studies have shown poor stability of 2D:3D mixed perovskites and 2D/3D stacking structure at a high temperature of 85°C, despite their promising stability at a lower temperature of 55°C [11]. To accelerate the operational aging process, the PSMs were subjected to simultaneous illumination and heat at 85°C (Figure 4b). Under these harsh conditions, the devices retained 90% of their initial PCE after 1600 h of operation. These results demonstrate that ATB can significantly improve the operational stability of PSMs. Simultaneously, the stability of encapsulated PSMs under 85°C/85% RH conditions was examined. As shown in Figure 4c, the ATB-treated device retained > 95% of its initial efficiency after 2000 h of damp-heat testing.

3 | Conclusion

In summary, we have realized high-efficiency perovskite modules with enhanced operational stability through adopting the functional ATB on perovskite surface to induce the in situ dual-stage reaction. We demonstrated that the first reaction between the ATB with formamidinium ions can effectively reduce surface defects and induce a n-type doping, which mainly attributes to improving PSM efficiency. The second cycled reaction mediated by thiol groups in ATB can continuously eliminate the I_2 and Pb^0 generated during the PSM aging, which mainly attributes to enhancing PSM operational stability. Consequently, the resulting PSMs achieved PCEs of 23.3% (11.2 cm^2, aperture area) and 21.2% (694.5 cm^2, aperture area), with exceptional operational stability retaining > 99% of their initial PCE after 2000 h under continuous 1-sun illumination at 25°C and > 90% PCE following 1600 h at 85°C. Our novel surface reaction engineering provides guidelines for the step-wisely and continuously regulate the perovskite surface to achieve high-performance and long-term stable PSMs, offering more opportunity to their commercialization.

Acknowledgments

This work is supported partially by the National Natural Science Foundation of China (grant nos. 52232008, 52102245, 52402254, 22409061, and 52533012), Beijing Natural Science Foundation (Z240024), Beijing Nova Program (20220484016), Young Elite Scientists Sponsorship Program by CAST (2022QNRC001), the project of China Three Gorges Corporation named key technologies of intelligent joint regulation and operation with grid connected friendly in power station group of wind, solar photovoltaic and energy storage (WWKY-2021-0173), Huaneng Group Headquarters Science and Technology Project (HNKJ20-H88), the Fundamental Research Funds for the Central Universities (2023MS042, 2024MS036, 2023MS047, 2024MS039, 2024JC005, and FRF-TP-25-05C), and the NCEPU "Double First-Class" Program, Beijing Natural Science Foundation (3252025).

Funding

This research was funded by the National Natural Science Foundation of China (grant nos. 52232008, 52102245, 52402254, 22409061, and 52533012), Beijing Natural Science Foundation (Z240024), Beijing Nova Program (20220484016), Young Elite Scientists Sponsorship Program by CAST (2022QNRC001), the project of China Three Gorges Corporation named key technologies of intelligent joint regulation and operation with grid connected friendly in power station group of wind, solar photovoltaic and energy storage (WWKY-2021-0173), Huaneng Group Headquarters Science and Technology Project (HNKJ20-H88), the Fundamental Research Funds for the Central Universities (2023MS042, 2024MS036, 2023MS047, 2024MS039, 2024JC005, and FRF-TP-25-05C), and the NCEPU "Double First-Class" Program, Beijing Natural Science Foundation (3252025).

Data Availability Statement

The data that support the findings of this study are available from the corresponding author upon reasonable request.

References

1. J. Han, K. Park, S. Tan, et al., "Perovskite Solar Cells," *Nature Reviews Methods Primers* 5 (2025): 3.

2. Y. Li, Z. Zheng, X. Zheng, et al., "Mutual Stabilization of Hybrid and Inorganic Perovskites for Photovoltaics," *eScience* 6 (2026): 100449.

3. Z. Xiong, Q. Zhang, K. Cai, et al., "Homogenized Chlorine Distribution for >27% Power Conversion Efficiency in Perovskite Solar Cells," *Science* 390 (2025): 638.

4. S. M. Park, M. Wei, J. Xu, et al., "Engineering Ligand Reactivity Enables High-Temperature Operation of Stable Perovskite Solar Cells," *Science* 381 (2023): 209.

5. F. H. Isikgor, S. Zhumagali, L. V. T. Merino, M. De Bastiani, I. McCulloch, and S. De Wolf, "Molecular Engineering of Contact Interfaces for High-Performance Perovskite Solar Cells," *Nature Reviews Materials* 8 (2023): 89.

6. S. Qu, Y. Li, H. Huang, et al., "Unveiling the Mutual Promotion Mechanism of Adjacent Vacancy Defects Enables High-Performance Perovskite Solar Cells," *Advanced Materials* 37 (2025): 2508643.

7. X. Fan, J. Chen, J. Wang, et al., "Efficient Rigid and Flexible Perovskite Solar Cells Using Strongly Adsorbed Molecules for Lattice Repair and Grain Boundary Mitigation," *Energy & Environmental Science* 18 (2025): 2905.

8. C. Shang, D. Qu, Z. Bao, et al., "Reducing Energetic Disorder for High-Efficiency Perovskite Solar Cells with Low Urbach Energy by in Situ NH_3 Generation," *Angewandte Chemie International Edition* 64 (2025): e202516464.

9. H. Zheng, G. Liu, X. Dong, et al., "Self-Regulated Bilateral Anchoring Enables Efficient Charge Transport Pathways for High-Performance Rigid and Flexible Perovskite Solar Cells," *Nano-Micro Letters* 17 (2025): 328.

10. N. Xu, X. Qi, Z. Shen, et al., "Point Defects in Metal Halide Perovskites," *Nature Reviews Physics* 7 (2025): 554.

11. M. Wang, Z. Shi, C. Fei, et al., "Ammonium Cations with High pKa in Perovskite Solar Cells for Improved High-Temperature Photostability," *Nature Energy* 8 (2023): 1229.

12. G. Li, Z. Zhang, B. Agyei-Tuffour, et al., "Stabilizing High-Efficiency Perovskite Solar Cells via Strategic Interfacial Contact Engineering," *Nature Photonics* 20 (2026): 55.

13. Z. Chu, B. Fan, Y. Zhao, et al., "Laser Annealing Enables Rapid, Degradation-Free Ambient Processing of Perovskite Solar Modules," *Science* 390 (2025): 905.

14. T. J. Silverman, M. G. Deceglie, I. Repins, et al., "Durability Research Is Pivotal for Perovskite Photovoltaics," *Nature Energy* 10 (2025): 934.

15. S. S. Shin, B.-W. Park, J. H. Noh, and S. I. Seok, "Interlayer Engineering in Metal Halide Perovskite Photovoltaics," *Nature Photonics* 20 (2026): 11.

16. F. Pei, S. Lin, Z. Zhang, et al., "Inhibiting Defect Passivation Failure in Perovskite for Perovskite/Cu(In, Ga)Se2 Monolithic Tandem Solar Cells with Certified Efficiency 27.35%," *Nature Energy* 10 (2025): 824.

17. Q. Liu, L. Ding, J. Fu, et al., "Enhancing the Efficiency and Stability of Inverted Perovskite Solar Cells and Modules through Top Interface Modification with N-type Semiconductors," *Angewandte Chemie International Edition* 64 (2025): e202416390.

18. Y. Wang, Y. Liu, X. Luo, et al., "Improved Solvent Systems for Commercially Viable Perovskite Photovoltaic Modules," *Science* 390 (2025): 1021.

19. J. Wang, G. Jin, Q. Zhen, C. He, and Y. Duan, "Bulk Passivation and Interfacial Passivation for Perovskite Solar Cells: Which One Is More Effective?," *Advanced Materials Interfaces* 8 (2021): 2002078.

20. C. Tian, A. Sun, J. Chen, et al., "Photostable Donor–acceptor Interface for Minimizing Energy Loss in Inverted Perovskite Solar Cells," *Nature Photonics*. (2026)

21. H. Zhu, S. Teale, M. N. Lintangpradipto, et al., "Long-Term Operating Stability in Perovskite Photovoltaics," *Nature Reviews Materials* 8 (2023): 569.

22. F. Igbari, M. Bilal, and Z. Li, "Strategies for Performance and Stability Advancement in Multicomponent Perovskite Photovoltaics," *Journal of Materials Chemistry A* 13 (2025): 32964.

23. Q. Jiang, J. Tong, Y. Xian, et al., "Surface Reaction for Efficient and Stable Inverted Perovskite Solar Cells," *Nature* 611 (2022): 278.

24. H. Tang, Y. Shen, G. Yan, L. Han, and Q. Han, "Confining Iodide Migration with Quantified Barrier for Durable Perovskite Solar Cells," *Nature Communications* 16 (2025): 9345.

25. X. Ren, J. Wang, Y. Lin, et al., "Mobile Iodides Capture for Highly Photolysis- and Reverse-Bias-Stable Perovskite Solar Cells," *Nature Materials* 23 (2024): 810.

26. N. Y. Nia, M. Zendehdel, B. Paci, et al., "Co-Crystal Engineering of a Two-Dimensional Perovskite Phase for Perovskite Solar Modules with Improved Efficiency and Stability," *Nature Energy* 11 (2026): 135.

27. N. Ahn and M. Choi, "Towards Long-Term Stable Perovskite Solar Cells: Degradation Mechanisms and Stabilization Techniques," *Advanced Science* 11 (2024): 2306110.

28. X. Zhu, X. Jiang, S. Fu, et al., "Rational Electrostatic Iodine Regulation for Photothermally Stable Perovskite Solar Cells," *Advanced Energy Materials* 15 (2025): e03666.

29. J. Ye, W. Sheng, J. He, et al., "Extending Shelf-Life of Two-Step Method Precursor Solutions through Targeted Regulation for Highly Efficient and Reproducible Perovskite Solar Cells," *Angewandte Chemie International Edition* 63 (2024): e202411708.

30. J. Hu, Q. Cai, Y. Lin, et al., "Molecular Press Annealing Enables Robust Perovskite Solar Cells," *Science* 391 (2026): 164.

31. D. N. Minh, M. A. Haque, F. Yang, et al., "The Reactive Nature of Formamidinium: Amine Passivation Induces Heterostructure Formation in Inverted Perovskite Cells," *Joule* 9 (2025)

Supporting Information

Additional supporting information can be found online in the Supporting Information section.